

Mid-infrared top-gated Ge/Ge_{0.82}Sn_{0.18} nanowire phototransistors

Lu Luo, Mahmoud RM Atalla, Simone Assali, Sebastian Koelling, and Oussama Moutanabbir

Department of Engineering Physics, École Polytechnique de Montréal, Montréal, C.P. 6079, Succ. Centre-Ville, Montréal, Québec, Canada H3C 3A7

Abstract

Achieving high crystalline quality Ge_{1-x}Sn_x semiconductors at Sn content exceeding 10% is quintessential to implementing the long sought-after silicon-compatible mid-infrared photonics. Herein, by using sub-20 nm Ge nanowires as compliant growth substrates, Ge_{1-x}Sn_x alloys with a Sn content of 18% exhibiting a high composition uniformity and crystallinity along a few micrometers in the nanowire growth direction were demonstrated. The measured bandgap energy of the obtained Ge/Ge_{0.82}Sn_{0.18} core/shell nanowires is 0.322 eV enabling the mid-infrared photodetection with a cutoff wavelength of 3.9 μm . These narrow bandgap nanowires were also integrated into top-gated field-effect transistors and phototransistors. Depending on the gate design, these demonstrated transistors were found to exhibit either ambipolar or unipolar behavior with a subthreshold swing as low as 228 mV/decade measured at 85 K. Moreover, varying the top gate voltage from -1 V to 5 V yields nearly one order of magnitude increase in the photocurrent generated by the nanowire phototransistor under a 2330 nm illumination. This study shows that the core/shell nanowire architecture with a super thin core not only mitigates the challenges associated with strain buildup ob-

served in thin films but also provides a promising platform for all-group IV mid-infrared photonics and nanoelectronics paving the way toward sensing and imaging applications.

Keywords: Mid-infrared photonics; Germanium-tin alloys; Silicon photonics; Nanowires; Sensing and imaging.

Introduction

Group IV $\text{Ge}_{1-x}\text{Sn}_x$ alloys is an emerging class of narrow direct bandgap semiconductors that has recently been attracting a great deal of attention as a versatile platform for silicon-compatible mid-wave infrared (MWIR) photonics and optoelectronics.¹ The indirect-to-direct bandgap crossover can be achieved in these materials at a strain-dependent Sn content typically in the 6~10 at.% range.²⁻⁴ However, controlling the growth of $\text{Ge}_{1-x}\text{Sn}_x$ above this critical content to cover the MWIR range has been facing major hurdles due to the low solid solubility of Sn in Ge (<1 at.%) and the large lattice mismatch between Ge and Sn ($\approx 14.7\%$). These limitations can be mitigated, to a certain extent, through nonequilibrium epitaxial growth processes introducing strain-relaxed $\text{Ge}_{1-x}\text{Sn}_x/\text{Ge}$ buffer layers.^{5,6} While lattice mismatch-induced high compressive strain can be partially relaxed by forming multiple step-graded layers, the highly defective bottom $\text{Ge}_{1-x}\text{Sn}_x$ layers can still severely degrade the device performance⁷⁻¹² in addition to limiting the thermal stability of the material.^{13,14} To circumvent the harmful effects of these extended defects, nanoscale $\text{Ge}_{1-x}\text{Sn}_x$ material systems have been proposed as an alternative platform.^{15,16} Indeed, $\text{Ge}_{1-x}\text{Sn}_x$ nanowires (NWs) were shown to provide an effective path to relax the lattice mismatch-induced compressive strain through the free sidewall facets without forming a high density of defects in the material.¹⁷⁻¹⁹ Besides, these nanoscale materials also provide additional degrees of freedom to engineer and control light-matter interaction and the related absorption and detection.²⁰⁻²⁴

$\text{Ge}_{1-x}\text{Sn}_x$ NWs reported in recent studies were synthesized using various methods including the vapor-liquid-solid (VLS),²⁵⁻²⁸ in-plane solution-liquid-solid (IPSL),^{29,30} microwave-assisted solution-liquid-solid growth,^{31,32} and top-down etching.^{33,34} However, these methods typically yield NWs with either low Sn content (below 10 at.%) or irregular shapes thus limiting their potential for MWIR device development. In this regard, Ge/ $\text{Ge}_{1-x}\text{Sn}_x$ core/shell NW growth emerged as a reliable approach to obtain nanoscale $\text{Ge}_{1-x}\text{Sn}_x$ alloys at a higher and more uniform Sn composition.³⁵⁻³⁸ In this process, the Ge core acts as a compliant

growth template, which facilitates the relaxation of the compressive strain, leading to an increased Sn content and higher uniformity^{37,39,40} thus enabling the development of innovative nanoscale MWIR emitters and detectors.^{37,38,41,42} For example, Ge/Ge_{1-x}Sn_x core/shell NWs with a sub-20 nm Ge core and x in the 0.06-0.18 range were recently demonstrated and integrated in photoconductive detectors allowing a tunable cutoff wavelength covering from 2.0 μm to 3.9 μm .³⁷ Although these NW photoconductors are straightforward to fabricate and can provide relatively high photoresponsivity and photoconductive gain due to the extended carrier lifetime, their high dark current still remains a major burden. Moreover, both the NW small size and the low energy of MWIR photons limit the NW photodetector absorption efficiency, thus making it harder to accurately detect weak signals. These limitations are further exacerbated in single NW photodetectors. Hence, it is highly critical to integrate individual NWs into photodetector configurations optimized to yield a reduced dark current. Such requirements can be met in device architectures such as junctionless phototransistors.^{43,44}

A junctionless phototransistor simply involves the introduction of a gate contact to control the conductivity of the NW channel between the drain and the source without forming a PN junction thus eliminating the need for post-growth doping and annealing that can be complicated for Ge_{1-x}Sn_x-based materials due to their metastable nature. The gate can deplete the NW from its majority carriers by providing a potential barrier, thus effectively reducing the dark current. The prevalent configuration for NW phototransistors is the back-gated phototransistor, yet it exhibits a limited gate control.^{45,46} To simultaneously solve all of these challenges, in this work a top-gated field-effect transistors (FETs) were fabricated by using narrow bandgap Ge/Ge_{0.82}Sn_{0.18} core/shell NWs and the phototransistor performance in the MWIR range was demonstrated. The FET devices exhibit either ambipolar or unipolar transistor behavior depending on the design of the gate which can fully or partially and asymmetrically cover the transistor channel. Subthreshold swing values as low as 833 mV/decade and 228 mV/decade were achieved at 300 K and 85 K, respectively. The

power-dependent and gate-modulated photocurrent at 2330 nm illumination demonstrate a stable performance of the NW phototransistors. These results highlight the potential of $\text{Ge}_{1-x}\text{Sn}_x$ nanoscale alloys as versatile building blocks for group IV nanoelectronics and MWIR nanophotonics.

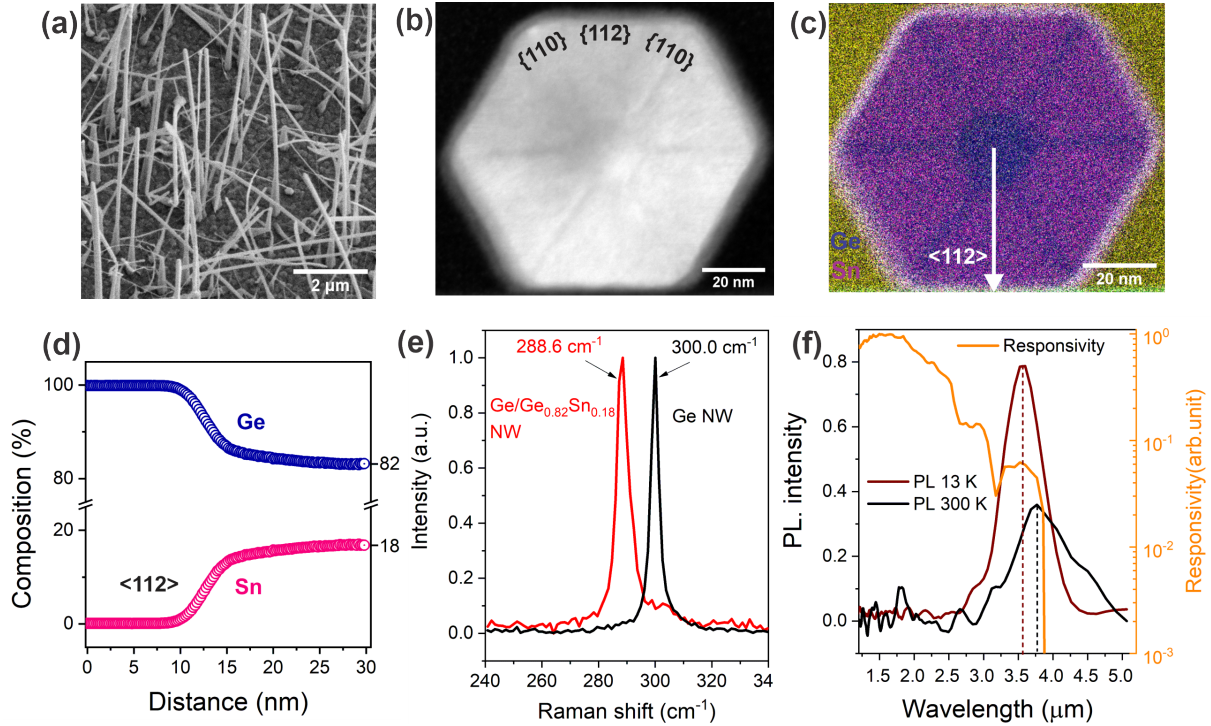


Figure 1: (a) SEM image of the as-grown $\text{Ge}/\text{Ge}_{0.82}\text{Sn}_{0.18}$ core/shell NWs. (b) Low magnification High-Angle Annular Dark-Field Scanning Transmission Electron Microscopy (HAADF-STEM) image showing the cross-section of the NW viewed along the $\langle 111 \rangle$ direction. (c) Energy dispersive X-Ray (EDX) elemental mapping of the NW cross-section. (d) Ge and Sn composition profiles along the $\langle 112 \rangle$ direction, indicated by the white arrow in (c), as measured by Atom Probe Tomography (APT). (e) Raman spectra of single $\text{Ge}/\text{Ge}_{0.82}\text{Sn}_{0.18}$ core/shell NW and Ge NW. (f) Photoluminescence spectra of the as-grown NW at 300 K and 85 K, and spectral responsivity of multiple NW device adapted from Ref.³⁷

Results

$\text{Ge}/\text{Ge}_{0.82}\text{Sn}_{0.18}$ core/shell NWs were grown on Ge(111) substrates in a reduced-pressure chemical vapor deposition (CVD) reactor following two growth steps. First, Ge core NWs

were grown at 340 °C by the VLS process, where 20 nm-diameter Au particles and GeH₄ served as the catalyst and the precursor, respectively. Second, Ge_{0.82}Sn_{0.18} shells with 35-40 nm in thickness were epitaxially grown at 260 °C on the obtained Ge NWs with the supply of GeH₄ and SnCl₄ precursors. Fig. 1(a) shows a scanning electron microscopy (SEM) image of the as-grown NWs with diameters and lengths in the range of 90-100 nm and 5-7 μm, respectively. Fig. 1(b) presents the low magnification high-angle annular dark-field scanning transmission electron microscopy (HAADF-STEM) image showing the NW cross-section viewed along the $\langle 111 \rangle$ direction. The energy dispersive X-ray (EDX) elemental map of the NW cross section is displayed in Fig. 1(c). A clear core/shell structure is observed arising from the Z-contrast of the image in Fig. 1(b). In addition, a 6-fold Sn-depleted substructure along the corners of the hexagonal GeSn shell (especially in the EDX image) is also visible, which corresponds to the $\{110\}$ crystal facets. This phenomenon is associated with facet-dependent capillarity diffusion due to the nonplanarity of the shell growth, which has been reported in group III-V-based NW heterostructures.^{47,48} Ge and Sn composition profiles measured by atom probe tomography (APT) along the $\langle 112 \rangle$ direction in the NW cross section are displayed in Fig. 1(d). The Sn composition increases rapidly from 0 to 15 at.% in the first 5 nm of the shell before reaching the targeted Sn content of 18 at.%. This rapid transition from Ge to Ge_{0.82}Sn_{0.18}, without a significant strain buildup in Ge_{0.82}Sn_{0.18} as shown below, is peculiar to the core/shell growth exploiting the compliant nature of the sub-20 Ge NW.³⁷

Raman spectroscopy measurements were performed on single NWs using a 633 nm excitation laser having a 0.7 μm-diameter spot size. A representative set of the recorded Raman spectra is shown in Fig. 1(e). It is noticeable that Ge-Ge LO phonon mode is shifted from 300.0 cm⁻¹ in Ge NW to 288.6 cm⁻¹ in Ge/Ge_{0.82}Sn_{0.18} core/shell NW suggesting that the latter are nearly fully relaxed. Indeed, the estimated residual strain is about -0.2% in these core/shell NWs, which is significantly below the -1.3% strain measured in Ge_{1-x}Sn_x pseudomorphic layers at similar content.^{5,49}

Photoluminescence (PL) measurements at 300 K and 13 K were recorded for as-grown Ge/Ge_{0.82}Sn_{0.18} core/shell NWs, as shown in Fig. 1(f). The description of the PL setup can be found in Methods. This figure also displays the responsivity spectrum of a multiple NW photoconductive device. The behavior of the latter is discussed in detail in Ref.³⁷ As expected, the peak wavelength red-shifts from 3.56 μm at 13 K to 3.77 μm at 300 K. The reduced bandgap energy at the high temperature results from the increased electron–phonon interactions and lattice expansion while the broader PL spectra at room temperature can result from the enhanced electron–phonon coupling.^{50,51} Note that the PL peak wavelength at room temperature is close to the measured cutoff wavelength (3.85 μm) of the photoconductive devices, providing an estimated bandgap energy of 0.322 eV at 300 K.

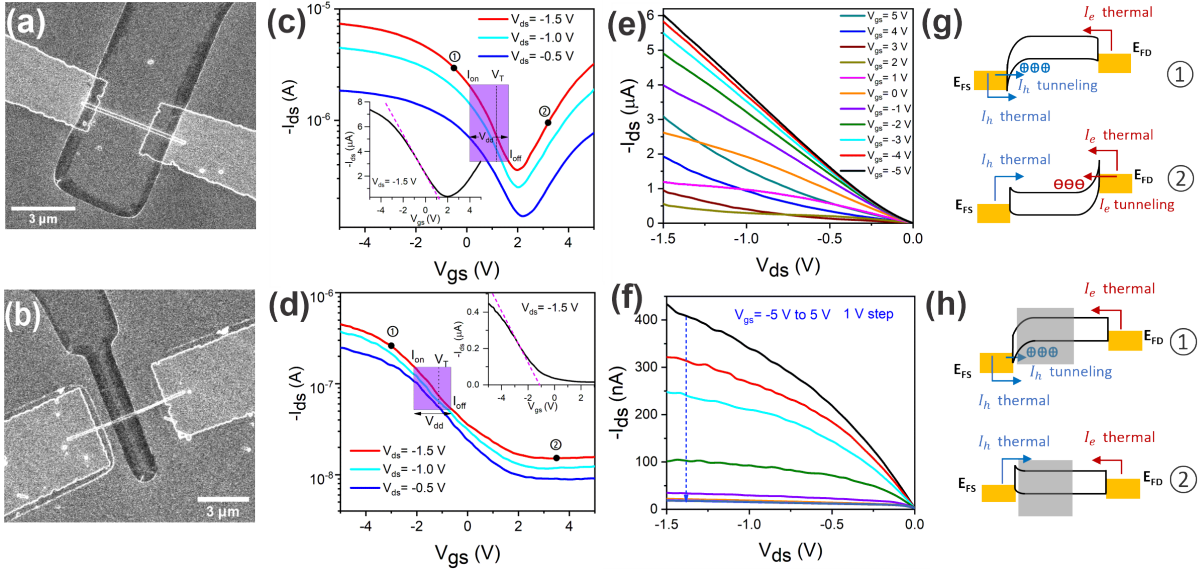


Figure 2: (a) and (b) Top view SEM images of devices A and B. (c) and (d) Logarithmic scale of I_{ds} - V_{gs} curves for device A and device B, respectively, the insets are the linear scale of I_{ds} - V_{gs} curve that was used to obtain the threshold voltages. (e) and (f) I_{ds} - V_{ds} curves for device A and device B respectively. (g) and (h) Band bending diagram explaining the ambipolar and unipolar transistor behavior of device A and B, respectively.

Top-gated FETs were fabricated (see Methods) to investigate the optoelectronic performance of the Ge/Ge_{0.82}Sn_{0.18} core/shell NWs. 20 nm-thick HfO₂ was deposited by atomic layer deposition (ALD) as the gate oxide. Two types of devices were fabricated: one with a

gate contact fully covering the NW (device A), and the other with a gate contact partially and asymmetrically covering the NW (device B). Fig. 2(a) and 2(b) are representative SEM images of device A and device B, where the gate length L is $2.7 \mu\text{m}$ and $1.3 \mu\text{m}$, respectively. The typical I_{ds} - V_{gs} curves of the two NW FETs at $V_{ds} = -0.5 \text{ V}$, -1.0 V , and -1.5 V are shown in Fig. 2(c) and 2(d). It is worth noting that the drain current I_{ds} in device A increases with both negative and positive gate voltages indicating p-type and n-type transfer properties with the p-type transfer as dominant. However, this ambipolar transistor behavior can be suppressed by the asymmetrical gate design, as the drain current I_{ds} in device B only increases with negative gate voltage suggesting a p-type FET behavior. The I_{ds} - V_{ds} output characteristic curves of the two devices with V_{gs} changing from -5 V to 5 V are exhibited in Fig. 2(e) and 2(f), showing the ambipolar and unipolar behavior. The observed ambipolarity arises from the narrow bandgap of $\text{Ge}_{0.82}\text{Sn}_{0.18}$ NW, which is also a common behavior in InSb NWs⁵² and black phosphorus FETs.⁵³

In a narrow bandgap material, the band bending can create a small triangular potential barrier in the metal-semiconductor interface where the electrons can easily tunnel through, therefore yielding a tunneling current. Besides, the electrons can be thermally excited through the Schottky barrier to form a thermal emission current.^{54,55} Therefore, the total drain current I_{ds} is the sum of the hole current I_h and electron current I_e including the contributions of both tunneling and thermionic emission for each carrier type. The thermionic emission current will always exist in a Schottky barrier, while the tunneling current becomes noticeable only when the triangular barrier width is sufficiently narrow. Fig. 2(g) exhibits the band diagrams at point 1 and point 2, marked in Fig. 2(c), describing the origin of the ambipolar transistor behavior of device A. Fig. 2(h) shows the band diagrams at point 1 and point 2, indicated in Fig. 2(d), illustrating the unipolar transistor behavior of device B. For the top-gated transistor with the channel fully covered by the gate contact, tunneling dominates the current when the gate voltage is raised positively (n-channel) or negatively (p-channel) due to the bent band at the metal-drain and metal-source interfaces.

The unipolar transfer behavior in device B is the result of the asymmetrical gate control. Due to the absence of the gate control, Fig. 2(h) shows that the band of the larger ungated region (right side) is more difficult to bend than that of the shorter ungated region (left side). Thus, the thermal emission current dominates on the drain side where not covered by the gate contact. When the gate voltage increases toward positive values, the electron tunneling current is blocked by the relatively thick barrier at the drain-metal interface.

The on/off ratio and subthreshold swing (SS) captures the off-state leakage and the switching speed, which are important parameters to evaluate the transistor performance. By following the method in,^{56,57} the on (I_{on}) and off (I_{off}) currents for a FET should be the values measured at $V_g=V_T-0.7V_{dd}$ and $V_g=V_T+0.3V_{dd}$ in the $I_{ds}-V_{gs}$ curve, respectively. V_{dd} is the power supply voltage which is equal to 1.5 V in this study, and V_T is the threshold voltage which is extracted using the standard peak transconductance method.⁵⁸ V_T for device A and device B is estimated at 1.2 V and -1.1 V and their on/off ratios are 4.6 and 2.8, respectively.

The SS values, defined as $R = [\frac{d(\log_{10}I_d)}{dV_g}]^{-1}$, were found to be respectively 1860 mV/decade and 3300 mV/decade for device A and device B, which are similar to those reported for InSb NWs^{52,59} InAs NW,⁶⁰ and black phosphorus FETs.⁵³ The low on/off ratio and the weak SS in both Ge/Ge_{0.82}Sn_{0.18} NW FETs result from the high off-state current. The high off-state current in a narrow bandgap NW FET can be attributed to several reasons including the gate leakage current, thermionic emission current (as mentioned above), trap-assisted tunneling (TAT) current, and ambipolar current.^{61,62} However, the first reason can be excluded because the measured gate leakage is less than 17 pA (as outlined in the Supplementary Information, Section 1), which is close to the noise level. This means that a uniform and conformal ALD-deposited dielectric layer was formed on the NW FETs, as shown in Fig. S2(a) and S2(b). Note that the off-state current in device B is ~ 3 to 10 times less than that of device A, indicating that the asymmetrical gate design can shrink the off-state current. Indeed, the high off-state current in device A is attributed to the ambipolar behavior. The same

phenomenon was reported in InAs NW and NW-based tunnel field-effect transistors.^{63,64} Both the thermionic emission and the TAT current are sensitive to temperature. The TAT current results from defects at the drain/channel interface, which can create energy levels within the bandgap and assist electrons in tunneling through the barrier.⁶² To evaluate the temperature dependence of the off-state current of Ge/Ge_{0.82}Sn_{0.18} NW FETs, transport measurements at low temperature were conducted in a cryogenic probe station (see Methods for details). Fig. 3(a) and 3(b) displays the transfer characteristic curves for the two devices measured at 300 K and 85 K at a drain voltage of -0.2 V and -0.5 V for the gate voltage ranging from -5 V to 5 V and -2 V to 8 V, respectively. The off-state current in both devices was largely reduced as expected, leading to an increased on/off ratio and a reduced SS value. Note that the devices in Fig. 3 are not the same devices as in Fig. 2.

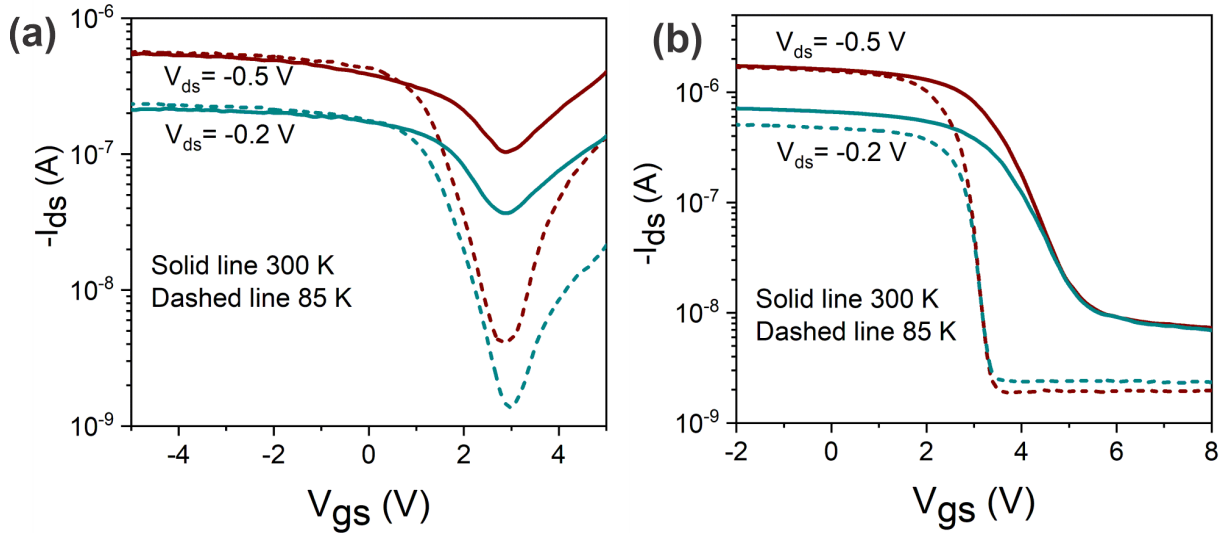


Figure 3: (a) I_{ds} - V_{gs} curves for device A at 300 K and 85 K. (b) I_{ds} - V_{gs} curves for device B at 300 K and 85 K

Following the calculation method mentioned above, the I_{on}/I_{off} ratio of device A and device B were found to increase from 1.57 and 3.5 at 300 K to 3.87 and 51.1 at 85 K, respectively. Simultaneously, both devices show a decrease in the SS value as the temperature is cooled down to 85 K from 2247 mV/decade to 664 mV/decade in device A and from 833 mV/decade to 228 mV/decade in device B. The SS is expected to change linearly with

temperature following $(\ln 10) \left(\frac{kT}{q} \right) \left(\frac{C_{ox} + C_d}{C_d} \right)$, where C_d and C_{ox} are depletion capacitance and gate oxide capacitance, and kT/q is the thermal voltage. The ratio of SS change in both devices is very close to the ratio of temperature change, which is 3.53.

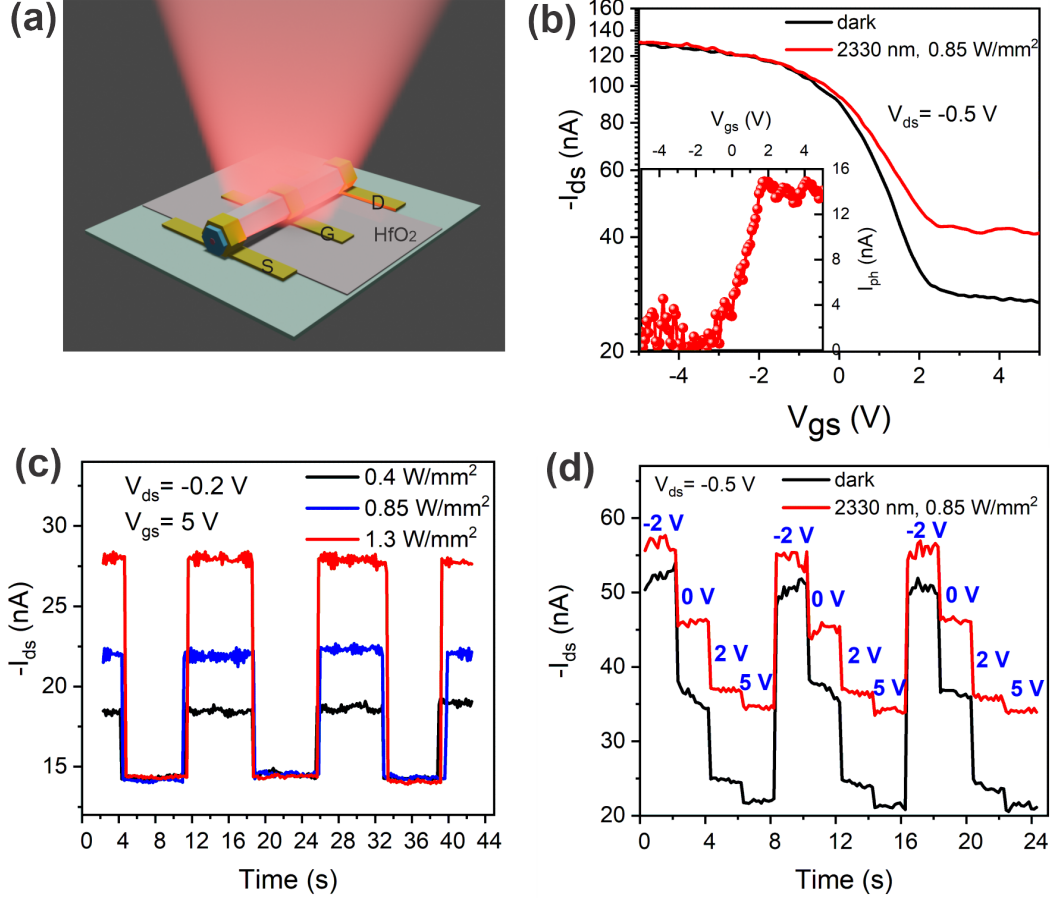


Figure 4: (a) Schematic illustration of the Ge/Ge_{0.82}Sn_{0.18} core/shell NW top-gated phototransistor. (b) I_{ds} - V_{gs} curves of the top-gated phototransistor under dark condition and 2330 nm illumination. The inset shows the measured photocurrent vs. the gate voltage. (c) Photocurrent of the top-gated phototransistor under 2330 nm laser at different power densities. (d) Time-resolved drain current at four different gate voltages under dark and 2330 nm illumination conditions.

The gate voltage modulated photoresponse performance of the Ge/Ge_{0.82}Sn_{0.18} NW phototransistor was also investigated at room temperature. The schematic of the phototransistor is illustrated in Fig. 4(a), where a 2330 nm laser diode was used as the light source. Fig. 4(b) depicts the I_{ds} - V_{gs} curves with and without illumination when the drain voltage V_{ds} is -0.5 V, and the inset displays the photocurrent I_{ph} versus V_{gs} extracted from Fig. 4(b).

A small photocurrent oscillating around 2 nA is detected when the gate voltage is below -1 V then increases gradually until it reaches saturation at 14 nA with the gate voltage increased from -1 V to 5 V. Fig. 4(c) shows the transient photocurrent at varied light intensities under the conditions of $V_{ds} = -0.2$ V and $V_{gs} = 5$ V. In Fig. 4(d), the transient drain current with and without light at different gate voltages are shown for $V_{ds} = -0.5$ V. The gate-modulated photocurrent in this figure is in good agreement with the behavior in Fig. 4(b). The power-dependent and gated-modulated photoresponse in Fig. 4(c) and 4(d) indicate a stable performance of the NW top-gated mid-infrared phototransistors. In fact, the top-gated NW FETs show a photoresponse and a gate modulation performance comparable to those of n-type InAs back-gated FET.⁶⁵ Additionally, in comparison to the side-gated NW FETs,⁶⁶ the top-gated NW FETs demonstrated in this work exhibit at least a 50 % increase in the on/off ratio and a 7-fold enhancement in photocurrent while being under 10 times lower light power density.

In conclusion, nanoscale $\text{Ge}_{0.82}\text{Sn}_{0.18}$ alloys with high crystallinity and content uniformity were achieved using sub-20 nm Ge NWs as compliant growth substrates. The obtained Ge/ $\text{Ge}_{0.82}\text{Sn}_{0.18}$ core/shell NWs have a bandgap energy of 0.322 eV allowing the mid-infrared photodetection with a cutoff wavelength of 3.9 μm . The grown NWs were also introduced in top-gated FETs exhibiting a strong ambipolar behavior with a small I_{on}/I_{off} ratio (less than 10). The ambipolar behavior and the off-state current of Ge/ $\text{Ge}_{0.82}\text{Sn}_{0.18}$ NW FETs can be reduced by introducing an asymmetrical top gate contact. Power-dependent and gate-modulated photoresponse under a 2330 nm laser illumination indicated a stable gate control in the NW top-gated phototransistors, which yielded at least a 50 % increase in the on/off ratio and a 7-fold enhancement in photocurrent under 10 times lower light power density as compared to the side-gated NW FETs. These results hint at the potential of nanoscale $\text{Ge}_{1-x}\text{Sn}_x$ semiconductors for all-group IV mid-infrared optoelectronics.

Methods

Fabrication of top-gated NW device. The as-grown NWs were drop-casted onto a Si substrate with a 100 nm-thick SiO₂ layer. Then methyl methacrylate (MMA) and poly methyl methacrylate (PMMA) were spin-coated on the SiO₂/Si substrate. EBL (Raith 150) was used to define drain and source patterns. Afterward, the sample was dipped into 5 % HCl solution for 30 s to remove the native oxide. The sample was subsequently transferred to an E-beam evaporator chamber quickly to deposit Cr/Au (5/150 nm). After the first lift-off, 20 nm of HfO₂ layer was deposited on the sample by ALD followed by a second EBL, metal deposition, and the liftoff procedures to form the top-gate contacts.

Photoluminescence setup. The NW sample was fixed on the sample holder inside the cryogenic chamber. A helium closed loop was installed to cool down the chamber. The excitation was carried out using an 808 nm laser focused on the sample using a 25x objective. The emission coming from the sample was fed into a Fourier-transform infrared spectrometer.

Low-temperature measurement setup. A cryogenic probe station from Janis Research Company was used to carry out low-temperature transport measurements. The chamber was evacuated by a mechanical pump, where the liquid Ni was introduced once the pressure reached 10⁸ Psi. The temperature in the chamber was controlled by a PID controller.

Acknowledgement

The authors thank J. Bouchard for the technical support with the CVD system. O.M. acknowledges support from NSERC Canada (Discovery, SPG, and CRD Grants), Canada Research Chairs, Canada Foundation for Innovation, Mitacs, PRIMA Québec, Defence Canada (Innovation for Defence Excellence and Security, IDEaS), the European Union's Horizon Europe research and innovation programme under grant agreement No 101070700 (MIRAQLS), the US Army Research Office Grant No. W911NF-22-1-0277, and the Air Force Office of

References

- (1) Moutanabbir, O.; Assali, S.; Gong, X.; O'Reilly, E.; Broderick, C.; Marzban, B.; Witzens, J.; Du, W.; Yu, S.-Q.; Chelnokov, A.; others Monolithic infrared silicon photonics: the rise of (Si) GeSn semiconductors. *Applied Physics Letters* **2021**, *118*, 110502.
- (2) Gupta, S.; Magyari-Köpe, B.; Nishi, Y.; Saraswat, K. C. Achieving direct band gap in germanium through integration of Sn alloying and external strain. *Journal of Applied Physics* **2013**, *113*.
- (3) Attiaoui, A.; Moutanabbir, O. Indirect-to-direct band gap transition in relaxed and strained Ge_{1-x}Si_xSn_y ternary alloys. *Journal of Applied Physics* **2014**, *116*, 063712.
- (4) Eckhardt, C.; Hummer, K.; Kresse, G. Indirect-to-direct gap transition in strained and unstrained Sn x Ge 1- x alloys. *Physical Review B* **2014**, *89*, 165201.
- (5) Assali, S.; Nicolas, J.; Mukherjee, S.; Dijkstra, A.; Moutanabbir, O. Atomically uniform Sn-rich GeSn semiconductors with 3.0–3.5 μ m room-temperature optical emission. *Applied Physics Letters* **2018**, *112*, 251903.
- (6) Dou, W.; Benamara, M.; Mosleh, A.; Margetis, J.; Grant, P.; Zhou, Y.; Al-Kabi, S.; Du, W.; Tolle, J.; Li, B.; others Investigation of GeSn strain relaxation and spontaneous composition gradient for low-defect and high-Sn alloy growth. *Scientific Reports* **2018**, *8*, 5640.
- (7) Buca, D.; Bjelajac, A.; Spirito, D.; Concepción, O.; Gromovy, M.; Sakat, E.; Lafosse, X.; Ferlazzo, L.; von den Driesch, N.; Ikonik, Z.; others Room Temperature Lasing in GeSn Microdisks Enabled by Strain Engineering. *Advanced Optical Materials* **2022**, *10*, 2201024.

- (8) Chrétien, J.; Thai, Q.; Frauenrath, M.; Casiez, L.; Chelnokov, A.; Reboud, V.; Hartmann, J.; El Kurdi, M.; Pauc, N.; Calvo, V. Room temperature optically pumped GeSn microdisk lasers. *Applied Physics Letters* **2022**, *120*, 051107.
- (9) Zhou, Y.; Miao, Y.; Ojo, S.; Tran, H.; Abernathy, G.; Grant, J. M.; Amoah, S.; Salamo, G.; Du, W.; Liu, J.; others Electrically injected GeSn lasers on Si operating up to 100 K. *Optica* **2020**, *7*, 924–928.
- (10) Atalla, M. R.; Assali, S.; Koelling, S.; Attiaoui, A.; Moutanabbir, O. High-bandwidth extended-SWIR GeSn photodetectors on silicon achieving ultrafast broadband spectroscopic response. *ACS Photonics* **2022**, *9*, 1425–1433.
- (11) Atalla, M. R.; Assali, S.; Koelling, S.; Attiaoui, A.; Moutanabbir, O. Dark current in monolithic extended-SWIR GeSn PIN photodetectors. *Applied Physics Letters* **2023**, *122*, 031103.
- (12) Tran, H.; Pham, T.; Margetis, J.; Zhou, Y.; Dou, W.; Grant, P. C.; Grant, J. M.; Al-Kabi, S.; Sun, G.; Soref, R. A.; others Si-based GeSn photodetectors toward mid-infrared imaging applications. *ACS Photonics* **2019**, *6*, 2807–2815.
- (13) Nicolas, J.; Assali, S.; Mukherjee, S.; Lotnyk, A.; Moutanabbir, O. Dislocation Pipe Diffusion and Solute Segregation during the Growth of Metastable GeSn. *Crystal Growth & Design* **2020**, *20*, 3493–3498.
- (14) Mukherjee, S.; Assali, S.; Moutanabbir, O. Atomic pathways of solute segregation in the vicinity of nanoscale defects. *Nano Letters* **2021**, *21*, 9882–9888.
- (15) Doherty, J.; Biswas, S.; Galluccio, E.; Broderick, C. A.; Garcia-Gil, A.; Duffy, R.; O’Reilly, E. P.; Holmes, J. D. Progress on germanium–tin nanoscale alloys. *Chemistry of Materials* **2020**, *32*, 4383–4408.

- (16) MS Windows NT Kernel Description. <https://irds.ieee.org/editions/2022/executive-summary>, Accessed: 2010-09-30.
- (17) Albani, M.; Assali, S.; Verheijen, M. A.; Koelling, S.; Bergamaschini, R.; Pezzoli, F.; Bakkers, E. P.; Miglio, L. Critical strain for Sn incorporation into spontaneously graded Ge/GeSn core/shell nanowires. *Nanoscale* **2018**, *10*, 7250–7256.
- (18) Kavanagh, K. L.; Saveliev, I.; Blumin, M.; Swadener, G.; Ruda, H. E. Faster radial strain relaxation in InAs–GaAs core–shell heterowires. *Journal of Applied Physics* **2012**, *111*.
- (19) Lewis, R. B.; Nicolai, L.; Kupers, H.; Ramsteiner, M.; Trampert, A.; Geelhaar, L. Anomalous strain relaxation in core–shell nanowire heterostructures via simultaneous coherent and incoherent growth. *Nano Letters* **2017**, *17*, 136–142.
- (20) Cao, L.; White, J. S.; Park, J.-S.; Schuller, J. A.; Clemens, B. M.; Brongersma, M. L. Engineering light absorption in semiconductor nanowire devices. *Nature Materials* **2009**, *8*, 643–647.
- (21) Cao, L.; Park, J.-S.; Fan, P.; Clemens, B.; Brongersma, M. L. Resonant germanium nanoantenna photodetectors. *Nano Letters* **2010**, *10*, 1229–1233.
- (22) Svensson, J.; Anttu, N.; Vainorius, N.; Borg, B. M.; Wernersson, L.-E. Diameter-dependent photocurrent in InAsSb nanowire infrared photodetectors. *Nano Letters* **2013**, *13*, 1380–1385.
- (23) Attiaoui, A.; Bouthillier, E.; Daligou, G.; Kumar, A.; Assali, S.; Moutanabbir, O. Extended Short-Wave Infrared Absorption in Group-IV Nanowire Arrays. *Phys. Rev. Appl.* **2021**, *15*, 014034.
- (24) Attiaoui, A.; Daligou, G.; Assali, S.; Skibitzki, O.; Schroeder, T.; Moutanabbir, O.

- Polarization-Tuned Fano Resonances in All-Dielectric Short-Wave Infrared Metasurface. *Advanced Materials* **2023**, *35*, 2300595.
- (25) Biswas, S.; Doherty, J.; Saladukha, D.; Ramasse, Q.; Majumdar, D.; Upmanyu, M.; Singha, A.; Ochalski, T.; Morris, M. A.; Holmes, J. D. Non-equilibrium induction of tin in germanium: towards direct bandgap Ge_{1-x}Sn_x nanowires. *Nature Communications* **2016**, *7*, 11405.
- (26) Doherty, J.; Biswas, S.; McNulty, D.; Downing, C.; Raha, S.; O'Regan, C.; Singha, A.; O'Dwyer, C.; Holmes, J. D. One-Step fabrication of GeSn branched nanowires. *Chemistry of Materials* **2019**, *31*, 4016–4024.
- (27) Doherty, J.; Biswas, S.; Saladukha, D.; Ramasse, Q.; Bhattacharya, T. S.; Singha, A.; Ochalski, T. J.; Holmes, J. D. Influence of growth kinetics on Sn incorporation in direct band gap Ge_{1-x}Sn_x nanowires. *Journal of Materials Chemistry C* **2018**, *6*, 8738–8750.
- (28) Seifner, M. S.; Dijkstra, A.; Bernardi, J.; Steiger-Thirsfeld, A.; Sistani, M.; Lugstein, A.; Haverkort, J. E.; Barth, S. Epitaxial Ge_{0.81}Sn_{0.19} nanowires for nanoscale mid-infrared emitters. *ACS Nano* **2019**, *13*, 8047–8054.
- (29) Azrak, E.; Chen, W.; Moldovan, S.; Gao, S.; Duguay, S.; Pareige, P.; Roca i Cabarrocas, P. Growth of In-Plane Ge_{1-x}Sn_x Nanowires with 22 at.% Sn Using a Solid–Liquid–Solid Mechanism. *The Journal of Physical Chemistry C* **2018**, *122*, 26236–26242.
- (30) Azrak, E.; Chen, W.; Moldovan, S.; Duguay, S.; Pareige, P.; Roca i Cabarrocas, P. Low-temperature plasma-assisted growth of core–shell GeSn nanowires with 30% Sn. *The Journal of Physical Chemistry C* **2019**, *124*, 1220–1226.
- (31) Barth, S.; Seifner, M. S.; Bernardi, J. Microwave-assisted solution–liquid–solid growth of Ge_{1-x}Sn_x nanowires with high tin content. *Chemical Communications* **2015**, *51*, 12282–12285.

- (32) Seifner, M. S.; Hernandez, S.; Bernardi, J.; Romano-Rodriguez, A.; Barth, S. Pushing the Composition Limit of Anisotropic Ge_{1-x}Sn_x Nanostructures and Determination of Their Thermal Stability. *Chemistry of Materials* **2017**, *29*, 9802–9813.
- (33) Eustache, E.; Mahjoub, M.; Guerfi, Y.; Labau, S.; Aubin, J.; Hartmann, J.; Bassani, F.; David, S.; Salem, B. Smooth plasma etching of GeSn nanowires for gate-all-around field effect transistors. *Semiconductor Science and Technology* **2021**, *36*, 065018.
- (34) Attiaoui, A.; Bouthillier, É.; Daligou, G.; Kumar, A.; Assali, S.; Moutanabbir, O. Extended Short-Wave Infrared Absorption in Group-IV Nanowire Arrays. *Physical Review Applied* **2021**, *15*, 014034.
- (35) Meng, A. C.; Fenrich, C. S.; Braun, M. R.; McVittie, J. P.; Marshall, A. F.; Harris, J. S.; McIntyre, P. C. Core-shell germanium/germanium–tin nanowires exhibiting room-temperature direct-and indirect-gap photoluminescence. *Nano Letters* **2016**, *16*, 7521–7529.
- (36) Assali, S.; Dijkstra, A.; Li, A.; Koelling, S.; Verheijen, M.; Gagliano, L.; Von Den Driessch, N.; Buca, D.; Koenraad, P.; Haverkort, J.; others Growth and optical properties of direct band gap Ge/Ge_{0.87}Sn_{0.13} core/shell nanowire arrays. *Nano Letters* **2017**, *17*, 1538–1544.
- (37) Luo, L.; Atalla, M. R.; Assali, S.; Koelling, S.; Daligou, G.; Moutanabbir, O. Mid-Infrared Detectors and Imagers Integrating All-Group IV Nanowires. 2023.
- (38) Kim, Y.; Assali, S.; Joo, H.-J.; Koelling, S.; Chen, M.; Luo, L.; Shi, X.; Burt, D.; Ikonik, Z.; Nam, D.; others Short-wave infrared cavity resonances in a single GeSn nanowire. *Nature Communications* **2023**, *14*, 4393.
- (39) Assali, S.; Albani, M.; Bergamaschini, R.; Verheijen, M. A.; Li, A.; Kölling, S.; Gagliano, L.; Bakkers, E. P.; Miglio, L. Strain engineering in Ge/GeSn core/shell nanowires. *Applied Physics Letters* **2019**, *115*.

- (40) Assali, S.; Bergamaschini, R.; Scalise, E.; Verheijen, M. A.; Albani, M.; Dijkstra, A.; Li, A.; Koelling, S.; Bakkers, E. P.; Montalenti, F.; others Kinetic control of morphology and composition in Ge/GeSn core/shell nanowires. *ACS Nano* **2020**, *14*, 2445–2455.
- (41) Luo, L.; Assali, S.; Atalla, M. R.; Koelling, S.; Attiaoui, A.; Daligou, G.; Martí, S.; Arbiol, J.; Moutanabbir, O. Extended-SWIR photodetection in all-group IV core/shell nanowires. *ACS Photonics* **2022**, *9*, 914–921.
- (42) Singh, S.; Mukherjee, S.; Mukherjee, S.; Assali, S.; Luo, L.; Das, S.; Moutanabbir, O.; Ray, S. K. Ge–Ge_{0.92}Sn_{0.08} core–shell single nanowire infrared photodetector with superior characteristics for on-chip optical Communication. *Applied Physics Letters* **2022**, *120*.
- (43) Roudsari, A. F.; Saini, S. S.; Nixon, O.; Anantram, M. Junction-less phototransistor with nanowire channels, a modeling study. *Optics Express* **2014**, *22*, 12573–12582.
- (44) Colinge, J.-P.; Kranti, A.; Yan, R.; Lee, C.-W.; Ferain, I.; Yu, R.; Akhavan, N. D.; Razavi, P. Junctionless nanowire transistor (JNT): Properties and design guidelines. *Solid-State Electronics* **2011**, *65*, 33–37.
- (45) Galluccio, E.; Doherty, J.; Biswas, S.; Holmes, J. D.; Duffy, R. Field-Effect Transistor Figures of Merit for Vapor–Liquid–Solid-Grown Ge_{1-x}Sn_x (x= 0.03–0.09) Nanowire Devices. *ACS Applied Electronic Materials* **2020**, *2*, 1226–1234.
- (46) Appenzeller, J.; Knoch, J.; Bjork, M. T.; Riel, H.; Schmid, H.; Riess, W. Toward nanowire electronics. *IEEE Transactions on Electron Devices* **2008**, *55*, 2827–2845.
- (47) Zheng, C.; Wong-Leung, J.; Gao, Q.; Tan, H. H.; Jagadish, C.; Etheridge, J. Polarity-driven 3-fold symmetry of GaAs/AlGaAs core multishell nanowires. *Nano Letters* **2013**, *13*, 3742–3748.

- (48) Rudolph, D.; Funk, S.; Doblinger, M.; Morkotter, S.; Hertenberger, S.; Schweickert, L.; Becker, J.; Matich, S.; Bichler, M.; Spirkoska, D.; others Spontaneous alloy composition ordering in GaAs-AlGaAs core-shell nanowires. *Nano Letters* **2013**, *13*, 1522–1527.
- (49) Bouthillier, É.; Assali, S.; Nicolas, J.; Moutanabbir, O. Decoupling the effects of composition and strain on the vibrational modes of GeSn semiconductors. *Semiconductor Science and Technology* **2020**, *35*, 095006.
- (50) Zhang, D.; Jia, T.; Dong, R.; Chen, D. Temperature-dependent photoluminescence emission from unstrained and strained GaSe nanosheets. *Materials* **2017**, *10*, 1282.
- (51) Varshni, Y. P. Temperature dependence of the energy gap in semiconductors. *Physica* **1967**, *34*, 149–154.
- (52) Dalekhan, B.; Göransson, D.; Thelander, C.; Li, K.; Xing, Y.; Maisi, V.; Xu, H. Ambipolar transport in narrow bandgap semiconductor InSb nanowires. *Nanoscale* **2020**, *12*, 8159–8165.
- (53) Du, Y.; Liu, H.; Deng, Y.; Ye, P. D. Device perspective for black phosphorus field-effect transistors: contact resistance, ambipolar behavior, and scaling. *ACS Nano* **2014**, *8*, 10035–10042.
- (54) Hutin, L.; Le Royer, C.; Tabone, C.; Delaye, V.; Nemouchi, F.; Aussenac, F.; Clavelier, L.; Vinet, M. Schottky barrier height extraction in ohmic regime: Contacts on fully processed GeOI substrates. *Journal of the Electrochemical Society* **2009**, *156*, H522.
- (55) Penumatcha, A. V.; Salazar, R. B.; Appenzeller, J. Analysing black phosphorus transistors using an analytic Schottky barrier MOSFET model. *Nature Communications* **2015**, *6*, 8948.
- (56) Chau, R.; Datta, S.; Doczy, M.; Doyle, B.; Jin, B.; Kavalieros, J.; Majumdar, A.; Metz, M.; Radosavljevic, M. Benchmarking nanotechnology for high-performance and

- low-power logic transistor applications. *IEEE Transactions on Nanotechnology* **2005**, *4*, 153–158.
- (57) Xiang, J.; Lu, W.; Hu, Y.; Wu, Y.; Yan, H.; Lieber, C. M. Ge/Si nanowire heterostructures as high-performance field-effect transistors. *Nature* **2006**, *441*, 489–493.
- (58) Schroder, D. K. *Semiconductor material and device characterization*; John Wiley & Sons, 2015.
- (59) Candebat, D.; Zhao, Y.; Sandow, C.; Koshel, B.; Yang, C.; Appenzeller, J. InSb nanowire field-effect transistors—Electrical characterization and material analysis. 2009 Device Research Conference. 2009; pp 13–14.
- (60) Li, T.; Shen, R.; Sun, M.; Pan, D.; Zhang, J.; Xu, J.; Zhao, J.; Chen, Q. Improving the electrical properties of InAs nanowire field effect transistors by covering them with Y₂O₃/HfO₂ layers. *Nanoscale* **2018**, *10*, 18492–18501.
- (61) Zhu, Y.; Hudait, M. K. Low-power tunnel field effect transistors using mixed As and Sb based heterostructures. *Nanotechnology Reviews* **2013**, *2*, 637–678.
- (62) Zhu, Y.; Mohata, D. K.; Datta, S.; Hudait, M. K. Reliability studies on high-temperature operation of mixed As/Sb staggered gap tunnel FET material and devices. *IEEE Transactions on Device and Materials Reliability* **2013**, *14*, 245–254.
- (63) Yang, W.; Pan, D.; Shen, R.; Wang, X.; Zhao, J.; Chen, Q. Suppressing the excess OFF-state current of short-channel InAs nanowire field-effect transistors by nanoscale partial-gate. *Nanotechnology* **2018**, *29*, 415203.
- (64) Verhulst, A. S.; Vandenberghe, W. G.; Maex, K.; Groeseneken, G. Tunnel field-effect transistor without gate-drain overlap. *Applied Physics Letters* **2007**, *91*.
- (65) Zhang, X.; Yao, X.; Li, Z.; Zhou, C.; Yuan, X.; Tang, Z.; Hu, W.; Gan, X.; Zou, J.;

Chen, P.; others Surface-states-modulated high-performance InAs nanowire phototransistor. *The Journal of Physical Chemistry Letters* **2020**, *11*, 6413–6419.

- (66) Yang, Y.; Wang, X.; Wang, C.; Song, Y.; Zhang, M.; Xue, Z.; Wang, S.; Zhu, Z.; Liu, G.; Li, P.; others Ferroelectric enhanced performance of a GeSn/Ge dual-nanowire photodetector. *Nano Letters* **2020**, *20*, 3872–3879.